Chapter 5

Compact computation of laminar flow past an impulsively started circular cylinder: a comparison with experimental results

5.1 Introduction

Fluid patterns around cylinders of circular and square cross-sections have drawn a great deal of attention over years due to their theoretical significance and pragmatic relevance. The historical development and numerical assessment of the flow past a square cylinder have been well documented in section 3.4.5. However, with the development of compact FD scheme to tackle circular geometries in the previous chapter, we are now interested to carry out the investigation of fluid flow past a circular cylinder. Although the flow past a circular cylinder is quite similar to that of a square cylinder as far as instabilities are concerned, there are significant distinctions in the separation process and the resulting dependency of aerodynamic forces and shedding frequency on the value of Re. Unlike in the case of square cylinder, the points of separation are not fixed for circular cylinder. Moreover, the width of the recirculation bubble behind the square cylinder is at least unit side length, whereas in case of a circular cylinder it is less than half a diameter which results in shorter and narrower region for the von Kármán vortex formation. These properties result in a quite different flow around a circular cylinder than the

flow around a cylinder with square cross-section. Besides, these problem exhibit all the fluid mechanics characteristics of incompressible viscous flow despite having the simplest geometry. Because of these engaging nature of the flow, such problems have been studied intensively by the CFD community over a long period of time. As a result of this a number of theoretical, numerical and experimental studies related to such problems can be found in the literature. Please refer to the documents [5, 177, 178] and the works cited there in.

The pioneering theoretical study related to uniform fluid flow around a circular cylinder were done by Blasius [8] back in 1908, using the concept of boundary layer theory. In this work, the investigation focused on the time of first separation, the time at which the fluid begins to separate from the surface the the cylinder. This theory was further carried over by various researchers [53, 128, 168, 172] considering the restricted case of infinite Reynolds number. In later time, many initial flow characteristics of this idea are described at higher Re values. In this regard the work of Wang [164], Collins and Dennis [21] deserve special mention. Although the results of these investigations were only achieved for a brief period of time in the initial stage of the flow, they accurately indicated the basic structure of the introductory position.

Since Roshko [125], experimental research on vortex shedding behind a circular cylinder have been quite popular. In his work, Roshko first divided the behaviour of the flow past a circular cylinder into four big regimes, sub-critical, critical, super-critical and trans-critical, depending on the value of the Reynolds number. Over the course of time several other visualization based experimental studies [10, 23, 24, 44, 112, 161, 169] have been carried out for various Reynolds numbers. It is important to mention here that in [10] development of primary and secondary vortices have been studied extensively in both qualitative and quantitative aspects for Reynolds numbers up to 10^4. In fact, this work reports the first experimental existence of secondary vortex phenomena, which rotates in the opposite direction from the main vortex as a result of the second separation of the flow. Even after the availability of numerous experimental, studies the detailed experimental knowledge on the unsteady flow field is rather limited owning to the difficulties involved in

taking measurements in such flows. Nevertheless, these experimental works have provided great insight to the formation of the unsteady wake. They also provide us with abundance of experimental results to be compared with the numerical solutions, and help in the development of computational methods to investigate the flow for Reynolds number hitherto unexplored in the experimental studies.

Apart from the theoretical and experimental studies there is another class of purely numerical schemes to simulate flow around a circular cylinder. Numerical schemes could potentially avoid some of the limitations associated with theoretical and experimental investigations and hence provide a vivid understanding into the physics of the flow. Thom [154] in 1933, for instance, initiated the numerical studies of the steady flow at $Re = 10$ and 20. He showed that the numerical solution deviated significantly from the approximated analytical solution but agreed well with the observed pattern. Kawaguti [82] then used an iterative numerical scheme and obtained the solution at $Re = 40$. Later in 1958, Payne [119] carried out numerical computations for $Re = 40$ and 100 to investigate the unsteady flow around the cylinder. However, the author forced the flow to be symmetrical around the equator of the cylinder and hence solution at $Re = 100$ did not exhibit the von Kármán vortex shedding. It was in the work of Hirota and Miyakoda [59] where first numerical evidence of Kármán vortex street was ever been reported. The problem has been studied in [12, 31, 40, 41, 43, 58, 69, 71, 72, 84, 87, 98, 99, 126] for Reynolds number between 10 and 10000. These investigations are primarily focused on the time evolution of unsteady separated vortex behind the cylinder.

A plenty of different HOC schemes have been employed to tackle this problem due to the higher accuracy and smaller working stencil. Although the majority of the schemes found in the literature are based on the well known discretization approaches: finite difference, finite volume and finite element [31, 43, 73, 98, 119], the higher-order compact FD schemes are gaining more popularity because of their ease of implementation. While the finite difference approach is well suitable for rectangular geometries, it possesses a great challenge while tackling circular geometries, where it is challenging to construct a body fitted coordinate system. Therefore, in most of the finite difference methods for the problem use the tra-

ditional transformation technique between physical plane and computational plane [31, 40, 41, 71, 72, 73, 74, 126]. Limited studies to develop higher order compact finite difference scheme that can work directly on polar grids without any grid transformation [26, 69, 123]. Nevertheless, few other classes of techniques such as the vortex method, hybrid vortex method, large eddy simulation (LES) method, Lattice Boltzmann (LB) method, smoothed-particle hydrodynamics (SPH) method have also been widely used as a tool for the simulation of such flows [12, 58, 84, 111].

The purpose of this investigation is to study the vortex dynamics behind a circular cylinder for a wide range of Reynolds numbers and to establish the versatile nature of the scheme developed in the previous chapter. We have employed the compact scheme that have been developed in Chapter 4 to solve the streamfunction-vorticity formulation of the 2D N-S equations in cylindrical polar coordinates. For low and moderate Re, the simulations are carried out until the flow becomes steady or it reaches a periodic state. However, the solution at the initial stage of the flow is computed in case of the higher values of Re. Detailed discussion on the flow structure for all the Reynolds number are provided. The qualitative and quantitative comparison reveals close proximity of the current solution with available numerical and experimental solutions.

5.2 Governing Equations

The problem considered here is incompressible, unsteady viscous flow over an impulsively started circular cylinder with unit radius ($R_0 = D/2 = 1$). At the upstream boundary (R_∞), we have considered an incoming flow with uniform freestream velocity U_∞. The flow is governed by the streamfunction-vorticity ($\tilde{\psi} - \tilde{\omega}$) formulation of incompressible N-S equations which in polar $(\tilde{r}, \theta)$ coordinates are given as

$$\begin{cases} \dfrac{\partial \tilde{\omega}}{\partial \tilde{t}} + \tilde{u}\dfrac{\partial \tilde{\omega}}{\partial \tilde{r}} + \dfrac{\tilde{v}}{\tilde{r}}\dfrac{\partial \tilde{\omega}}{\partial \theta} = \nu\left(\dfrac{\partial^2 \tilde{\omega}}{\partial \tilde{r}^2} + \dfrac{1}{\tilde{r}}\dfrac{\partial \tilde{\omega}}{\partial \tilde{r}} + \dfrac{1}{\tilde{r}^2}\dfrac{\partial \tilde{\omega}}{\partial \theta^2}\right), & \text{(5.1a)} \\ \tilde{\omega} = -\left(\dfrac{\partial^2 \tilde{\psi}}{\partial \tilde{r}^2} + \dfrac{1}{\tilde{r}}\dfrac{\partial \tilde{\psi}}{\partial \tilde{r}} + \dfrac{1}{\tilde{r}^2}\dfrac{\partial^2 \tilde{\psi}}{\partial \theta^2}\right), & \text{(5.1b)} \end{cases}$$

where tilde sign ($\sim$) denotes the dimensional quantities. The radial velocity $\tilde{u} = \frac{1}{\tilde{r}}\frac{\partial \tilde{\psi}}{\partial \theta}$ and tangential velocity $\tilde{v} = -\frac{\partial \tilde{\psi}}{\partial \tilde{r}}$.

The nondimensional counterparts of the flow variables in the above-mentioned equations are obtained from

$$r = \frac{\tilde{r}}{R_0}, \quad t = \frac{\tilde{t}U_\infty}{R_0}, \quad \psi = \frac{\tilde{\psi}}{U_\infty R_0},$$

$$\omega = \frac{\tilde{\omega}R_0}{U_\infty}, \quad u = \frac{\tilde{u}}{U_\infty}, \quad v = \frac{\tilde{v}}{U_\infty},$$

along with the Reynolds number, for this problem, defined as $Re = U_\infty D/\nu$ following [10, 40]. Therefore, the N-S equations in nondimensional form become

$$\begin{cases} \dfrac{\partial \omega}{\partial t} + u\dfrac{\partial \omega}{\partial r} + \dfrac{v}{r}\dfrac{\partial \omega}{\partial \theta} = \dfrac{2}{Re}\left(\dfrac{\partial^2 \omega}{\partial r^2} + \dfrac{1}{r}\dfrac{\partial \omega}{\partial r} + \dfrac{1}{r^2}\dfrac{\partial^2 \omega}{\partial \theta^2}\right), & \text{(5.2a)} \\ \omega = -\left(\dfrac{\partial^2 \psi}{\partial r^2} + \dfrac{1}{r}\dfrac{\partial \psi}{\partial r} + \dfrac{1}{r^2}\dfrac{\partial^2 \psi}{\partial \theta^2}\right). & \text{(5.2b)} \end{cases}$$

5.3 Schematic of the problem and numerical issues

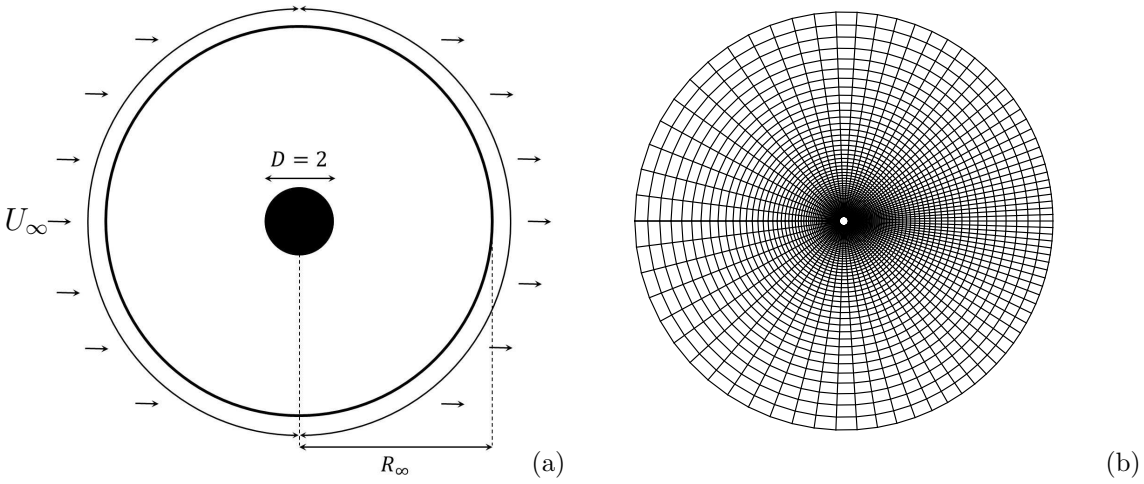

Fig. 5.1: (a) Flow configuration and (b) typical 61×81 nonuniform grid with $\lambda_\theta = 0.6$.

The 2D flow configuration of the problem is shown in Fig. 5.1a. The cylinder is placed at the centre of the circular domain. Following [43], we have set the far-field boundary at a distance $R_\infty = 45R_0$. On the solid surface $r = R_0$, the boundary

conditions for velocity components are those of no-slip conditions, i.e. $u = v = 0 \implies \psi = 0$. In the far stream $r = R_\infty$ in front of the cylinder, the potential flow is prescribed a unit value $u = U_\infty = 1$. For this problem, where the simulation results in periodic vortex shedding, we have imposed the convective boundary conditions $\phi_t + U_\infty \phi_r = 0$ (where ϕ represents ψ, u or v) at the downstream boundary, to capture the shedding process efficiently. In the direction of the flow, the convective boundary conditions can best facilitate continuous shedding of vortices when they leave the computational domain [12, 72, 91, 167]. In addition, at the inner boundary, vorticity may be derived by making use of the fact that $\psi = 0$, $\psi_r = 0$ on $r = R_0$ in equation (5.2b). The vorticity gradients at all the boundaries are computed using one-sided approximations already suggested in previous chapters.

The second-order compact scheme for the unsteady, incompressible N-S equations developed in Chapter 4 can work on nonuniform polar grids without any domain transformation. The proposed scheme renders equation (5.2a) to fully discretized form as follows,

$$\begin{aligned}
&\left(\frac{Re}{\delta t} + \widehat{C}_1\right)\omega_{i,j}^{n+1} - \widehat{C}_2\omega_{i+1,j}^{n+1} - \widehat{C}_3\omega_{i-1,j}^{n+1} - \widehat{C}_4\omega_{i,j+1}^{n+1} - \widehat{C}_5\omega_{i,j-1}^{n+1} \\
=&\left(\frac{Re}{\delta t} - \widehat{C}_1\right)\omega_{i,j}^{n} + \widehat{C}_2\omega_{i+1,j}^{n} + \widehat{C}_3\omega_{i-1,j}^{n} + \widehat{C}_4\omega_{i,j+1}^{n} + \widehat{C}_5\omega_{i,j-1}^{n} \\
&- \widehat{C}_6\left(\omega_{r_{i+1,j}}^{n+1} - \omega_{r_{i-1,j}}^{n+1}\right) - \left(\widehat{C}_7 + \frac{Re}{2r_i}\psi_{\theta i,j}^{n+1} - \frac{1}{r_i}\right)\omega_{r_{i,j}}^{n+1} \\
&- \widehat{C}_8\left(\omega_{\theta_{i,j+1}}^{n+1} - \omega_{\theta_{i,j-1}}^{n+1}\right) - \left(\widehat{C}_9 - \frac{Re}{2r_i^3}\psi_{r\,i,j}^{n+1}\right)\omega_{\theta_{i,j}}^{n+1} \\
&- \widehat{C}_6\left(\omega_{r_{i+1,j}}^{n} - \omega_{r_{i-1,j}}^{n}\right) - \left(\widehat{C}_7 + \frac{Re}{2r_i}\psi_{\theta i,j}^{n} - \frac{1}{r_i}\right)\omega_{r_{i,j}}^{n} \\
&- \widehat{C}_8\left(\omega_{\theta_{i,j+1}}^{n} - \omega_{\theta_{i,j-1}}^{n}\right) - \left(\widehat{C}_9 - \frac{Re}{2r_i^3}\psi_{r\,i,j}^{\;n}\right)\omega_{\theta_{i,j}}^{n},
\end{aligned} \tag{5.3}$$

and

$$\begin{aligned}
&\widehat{C}_1\psi_{i,j}^{n+1} - \widehat{C}_2\psi_{i+1,j}^{n+1} - \widehat{C}_3\psi_{i-1,j}^{n+1} - \widehat{C}_4\psi_{i,j+1}^{n+1} - \widehat{C}_5\psi_{i,j-1}^{n+1} \\
=&\omega_{i,j}^{n+1} - \widehat{C}_6\psi_{i,j}^{n+1}\left(\psi_{r_{i+1,j}}^{n+1} - \psi_{r_{i-1,j}}^{n+1}\right) - \left(\widehat{C}_7 - \frac{1}{r_i}\right)\psi_{r_{i,j}}^{n+1} \\
&- \widehat{C}_8\left(\psi_{\theta_{i,j+1}}^{n+1} - \psi_{\theta_{i,j-1}}^{n+1}\right) - \widehat{C}_9\psi_{\theta_{i,j}}^{n+1}
\end{aligned} \tag{5.4}$$

respectively.

The values of $\widehat{C}_i$'s are explained in section 4.2. Theoretically the scheme is at least

second-order accurate in space and has a Crank-Nicolson type second-order temporal accuracy. A nonuniform polar grid is generated in the domain $\Omega = [R_0, R_\infty] \times [0, 2\pi]$. In the θ-direction the grid points are clustered in Kármán vortex street region making sufficient changes in equation (4.32) and setting the parameters $L_\theta = 2\pi$ and $\lambda_\theta = 0.4$. For this problem, more grid points are accumulated near the cylinder surface in the r-direction using the function,

$$r_i = \exp\left(\frac{\lambda i}{n_r}\right),$$

where the parameter λ has the same values as the outer radius R_∞ of the computational domain. A nonuniform grid of size 61×81 thus formed has been shown in Fig. 5.1b.

Here, we calculate the drag (C_D) and lift coefficients (C_L) using the equations (4.45) and (4.46) mentioned in the previous chapter.

5.4 Numerical results and discussions

Investigations of laminar flows across a circular cylinder have established the fact that the flow stays irrotational everywhere immediately after the fluid motion is commenced. As fluid motion progresses, vorticity is generated on the cylinder wall which transports to the rear stagnation point where we see the first separation. Momentarily after the time of first separation for flows with $Re > 5$, a recirculating region develops as a result of flow reversal and it continuous to grow leading to two symmetrical vortices. No visible flow distortion takes place for flows with $Re \leq 5$ which has also been confirmed by the present investigation. Although the boundary layer separates from the cylinder at $Re \approx 6$, the flow remains steady and laminar. A thorough review of literature reveals that there is a value of the Reynolds number known as the critical Reynolds number (Re_c) and beyond this value the flow turns unsteady [10, 23, 31, 40, 98, 126]. Numerical studies indicates this Re_c to lie between 43 and 50, where the Hopf bifurcation occurs. For $Re > Re_c$, the flow shows periodic shedding of vortices, characterised by the von Kármán vortex street. The flow becomes more complicated with further increase in Reynolds number as the

secondary and tertiary vortices start to appear. Taking all these points into account and devolving on the attribute observed within each range, our study is divided into the following parts for $10 \leq Re \leq 9500$,

A. Flows for $10 \leq Re \leq 40$, well-known as steady-state region.

B. Flows for $100 \leq Re \leq 300$, wherein the wake behind the cylinder becomes unsteady. The wake oscillation grows in amplitude and finally creates sequence of periodic vortices referred to as the von Kármán vortex street.

For $Re > 300$, we consider flow close to the cylinder only on the early span of the simulation.

C. Flows for $300 < Re \leq 550$, where flow properties are unsteady, secondary eddies develop at the beginning but do not split up further. The flow is characterised by the occurrence of (i) bulge phenomena and (ii) isolated secondary vortex.

D. Flows for $1000 \leq Re \leq 9500$, which is characterised by the most complicated secondary α- and β-phenomena and tertiary sub-α- and sub-β-phenomena.

A. Flows for $10 \leq Re \leq 40$

It has already been mentioned that for $10 \leq Re \leq Re_c$ two symmetrical vortices are developed behind the cylinder and they grow with time till the flow reaches a steady state. This regime has been studied extensively by fluid dynamics researchers over the years using both steady as well as transient codes. Here, two flow separates from the cylinder wall and two counter rotating symmetric vortices are formed at the backside of the cylinder, known as the recirculating bubbles. These vortices grow with time in wake length L, the distance between the points A and B on the horizontal axis $\theta = 0$ and in angle of separation θ_s. The pictorial explanations of L and θ_s can be found in Fig. 5.2. Finally, as the flow reaches a steady state these vortices settle down in form of a wake. The physical properties of the wake finally developed depend on the Re under consideration. For the present study the

flows are simulated for $Re = 10$, 20 and 40. In Fig. 5.3, we have shown the steady-state streamlines and respective vorticity contours for different Re's. We can see the evolution of a stationary recirculating bubble behind the cylinder in each case. From the steamlines presented, it is amply clear that the size of these recirculating regions increase with the increase in Re values. The time evolution of C_D is presented in Fig. 5.4a which eventually establishes the steady nature of the flow for the Re values considered here.

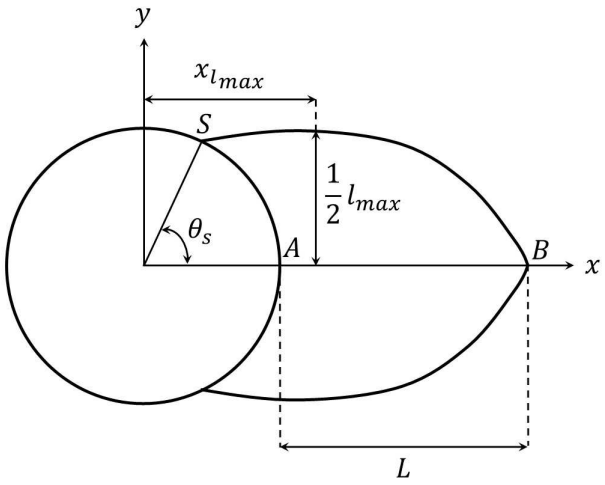

Fig. 5.2: Geometrcial parameters.

Table 5.1: Grid-independence of the numerical results on three different grids for steady-state flows.

	$Re = 10$			$Re = 20$			Re=40		
Grid	G1	G2	G3	G1	G2	G3	G1	G2	G3
L	0.498	0.501	0.516	1.830	1.832	1.832	4.450	4.395	4.448
θ_s	28.821	28.821	28.821	43.176	43.176	43.196	53.027	53.703	53.027
C_D	2.694	2.688	5.683	2.056	2.063	2.066	1.530	1.534	1.538

We then carry out the grid-independence study of the numerical results. In Table 5.1, we compare the parameters L, θ_s and C_D on nonuniform polar grids of three different sizes G1:65×97, G2:97×129 and G3:129×193 with $\delta t = 0.01$ for each computation. Besides, we have also shown the distribution of vorticities computed using grids G1, G2 and G3 over the surface of the cylinder for $Re = 40$ in Fig. 5.4b.

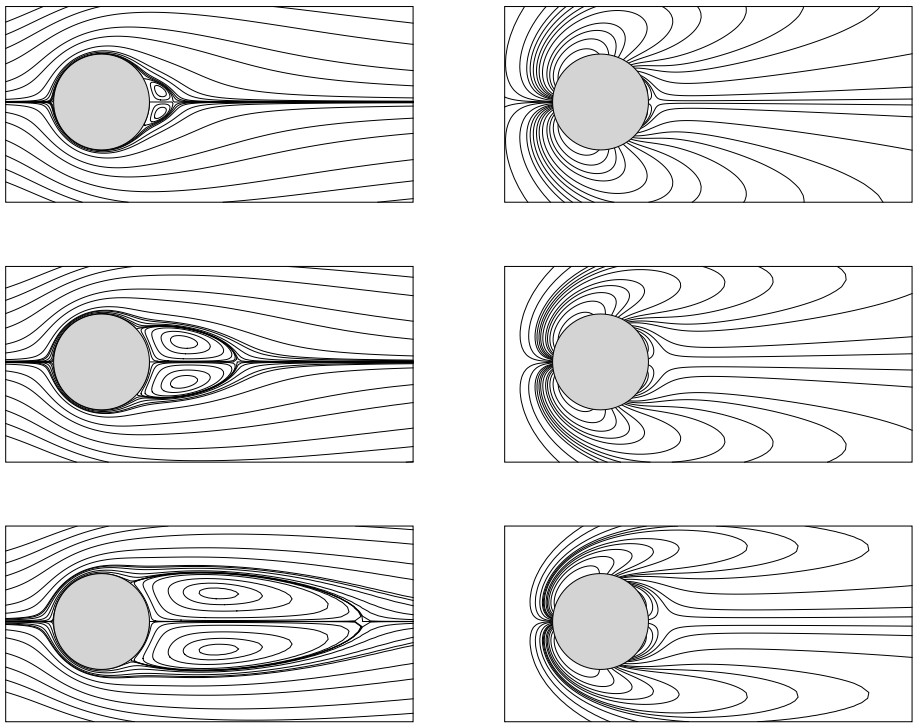

Fig. 5.3: Steady-state steamline (left) and vorticity (right) contours: (a) $Re = 10$, (b) $Re = 20$, (c) $Re = 40$.

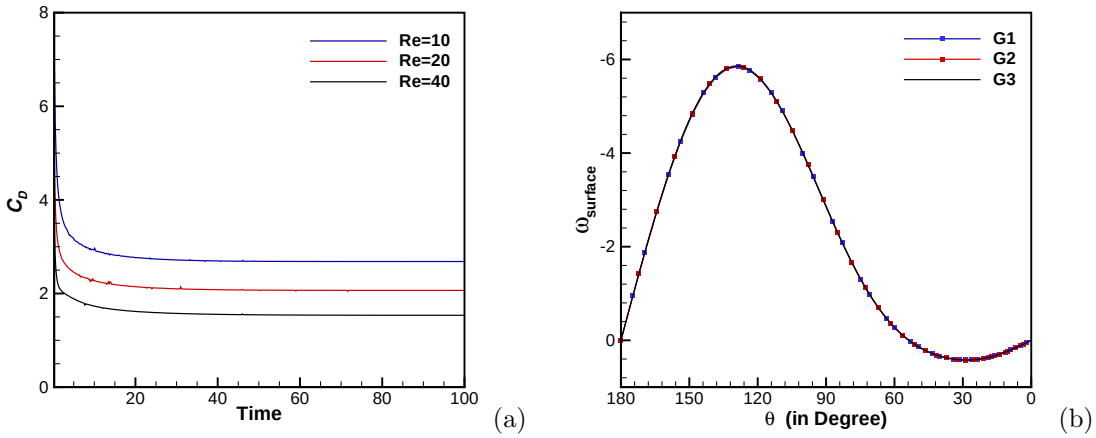

Fig. 5.4: (a) Evolution of C_D with time for $Re = 10$, 20 and 40; (b) Distribution of vortcity at steady state along the entire surface of the cylinder for $Re = 40$.

These analysis confirms the independency of our numerical solutions on grid size and indicates that a grid of size 129×193 is sufficient for accurate resolution of these flows. A comparison of the values of the parameters L, θ_s and C_D computed in the

Table 5.2: Comparison of L, θ_s and C_D at steady state for different Re.

		L	%-diff.	θ_s	%-diff.	C_D	%-diff.
Re=10	[58]	0.474	8.86	26.89	7.18	3.170	15.36
	[132]	0.504	2.38	29.732	3.06	2.699	0.59
	[87]	0.531	2.82	29.69	2.96	2.690	0.26
	Present	0.516		28.821		2.683	
Re=20	[24]	1.86	1.51	44.4	2.71		
	[58]	1.842	0.54	42.96	0.55	2.152	4.00
	[111]	1.92	4.58	42.79	0.95	2.111	2.13
	[127]	1.77	3.50	41.3277	4.52	2.0597	0.31
	[69]	1.8331	0.06	42.9248	0.63	2.0193	2.31
	[132]	1.851	1.03	43.141	0.13	1.949	6.00
	[87]	1.874	2.24	42.66	1.26	2.160	4.35
	Present	1.832		43.196		2.066	
Re=40	[24]	4.38	1.56	53.4	1.04		
	[58]	4.49	0.94	52.84	0.01	1.499	2.60
	[111]	4.51	1.37	52.84	0.01	1.574	2.29
	[127]	4.21	5.65	51.0249	3.57	1.5308	0.47
	[69]	4.4135	0.78	51.3012	3.01	1.5145	1.55
	[132]	4.625	3.83	53.226	0.72	1.439	6.88
	[87]	4.278	3.97	53.08	0.44	1.576	2.41
	Present	4.448		52.844		1.538	

present study, with well established numerical and experimental studies [24, 58, 69, 87, 111, 127, 132] is presented in Table 5.2. The table also contains the %-difference between the present data with the data taken from literature. Furthermore, the surface distribution of the post processed vorticity of the present simulation with those of references [31, 40] are shown in Fig. 5.5. It is heartening to see that the numerical results obtained in the present study are in line with the experimental and numerical results taken from the literature, both quantitatively and qualitatively.

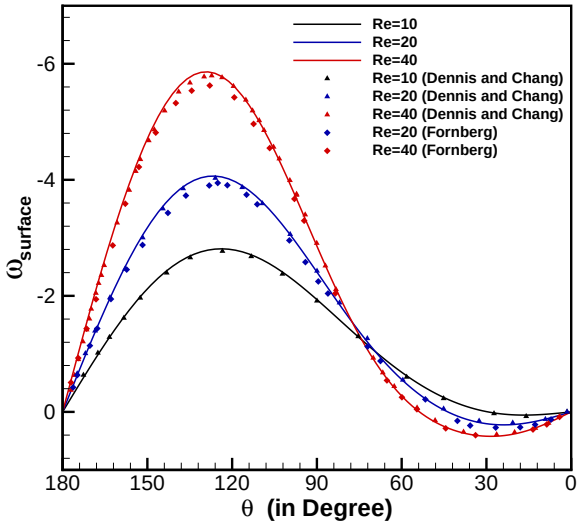

Fig. 5.5: Comparison of the surface distribution of vorticity for low Re's with existing results [31, 40].

B. Flows for $100 \leq Re \leq 300$

Earlier researches have confirmed that for $Re \geq Re_c$ the flow around a circular cylinder eventually becomes periodic in nature and develops vortex shedding behind the cylinder popularly represented by von Kármán vortex street. In this section, we have chosen $Re = 100$, 200 and 300 which typically exhibits this phenomenon. For the flow patterns of this range of Re, the recirculating zone behind the cylinder evolves quickly due to the rapid growth of velocities with time and the development of secondary vortices. The wake gains in size and strength as time progresses. The evolution of the maximum width l_{max} and the corresponding abscissa $x_{l_{max}}$ of the recirculating bubble (see Fig. 5.2) for $Re = 200$ has been compiled in Table 5.3. We also provide the experimental values of these parameters given by Bouard and Coutanceau [10] in this table. Very close match can be seen between the numerical and experimental solutions in all the cases.

As the flow evolves, it passes through different phases to eventually develop periodic vortex shedding. We have shown these stages for $Re = 100$ in Fig. 5.6, which shows the streamlines at different instants of the flow. Shortly after the flow

Table 5.3: Comparison of numerical values of l_{max} and $x_{l_{max}}$ for various Re and t with experimental results from [10] (within the parenthesis).

$t \rightarrow$		1.0	1.5	2.0	2.5	3.0
$Re = 200$	$x_{l_{max}}/D$	0.38	0.55	0.71	0.78	0.88
		(0.35)	(0.51)	(0.65)	(0.76)	(0.86)
	l_{max}/D	0.94	1.01	1.06	1.12	1.16
		(0.94)	(0.97)	(1.02)	(1.07)	(1.10)
$Re = 550$	$x_{l_{max}}/D$	0.26	0.48	0.64	0.74	0.81
		(0.30)	(0.50)	(0.66)	(0.76)	(0.85)
	l_{max}/D	0.96	1.00	1.06	1.12	1.18
		(0.94)	(0.98)	(1.03)	(1.10)	(1.16)
$Re = 3000$	$x_{l_{max}}/D$	0.18	0.31	0.34	0.71	0.78
		(0.19)	(0.26)	(0.40)	(0.73)	(0.84)
	l_{max}/D	0.99	1.02	1.10	1.16	1.22
		(0.93)	(0.98)	(1.04)	(1.11)	(1.20)

has started, a pair of symmetric eddies develop behind the cylinder (Fig. 5.6a–5.6c). As can be seen in Fig. 5.7a, soon after the flow is started impulsively C_D attains a very high value which in the course of the time begins to fall. During this process the vortices start to grow in size as well (Fig. 5.6a–5.6d). As the flow settles down, a partially steady state is reached with $C_L = 0$, the span of this state decreasing as the value of Re increases. From Fig. 5.6d onwards, appearance of some small fluctuation in the streamline is seen to be set up at the trail of the eddy, which eventually destroys the symmetry of the flow about $\theta = 0$ line. For $Re = 100$, this phenomena can be seen at around $t = 55$ in Fig. 5.7a. This particular instant is know as the first bifurcation point, which is lesser for higher values of Reynolds number (Fig. 5.11). At this stage, the eddies behind the cylinder gradually start to oscillate (Fig. 5.6e–5.6h) and the flow begins to exert a nonzero lift force on the cylinder. Shortly thereafter, vortices start shedding periodically resulting in the von Kármán vortex street. Over time, until a limiting condition is reached, the vortex shedding frequency increases. The drag coefficient increases once again as vortex shedding occurs, as the flow fully develops, both the drag and lift coefficients ultimately reach a periodic state (Fig. 5.7a). The periodicity of vortex shedding is further confirmed

by the single dominant peak for both C_D and C_L in the spectral density analysis presented in Fig. 5.7b. The flows for $Re = 200$ and 300 undergo the same evolution process described here although the duration of the phases varies with the value of Re. It is imperative to mention here that for all the values of Re considered in this section, the asymmetry of the flow sets in spontaneously without any artificial perturbation technique being introduced.

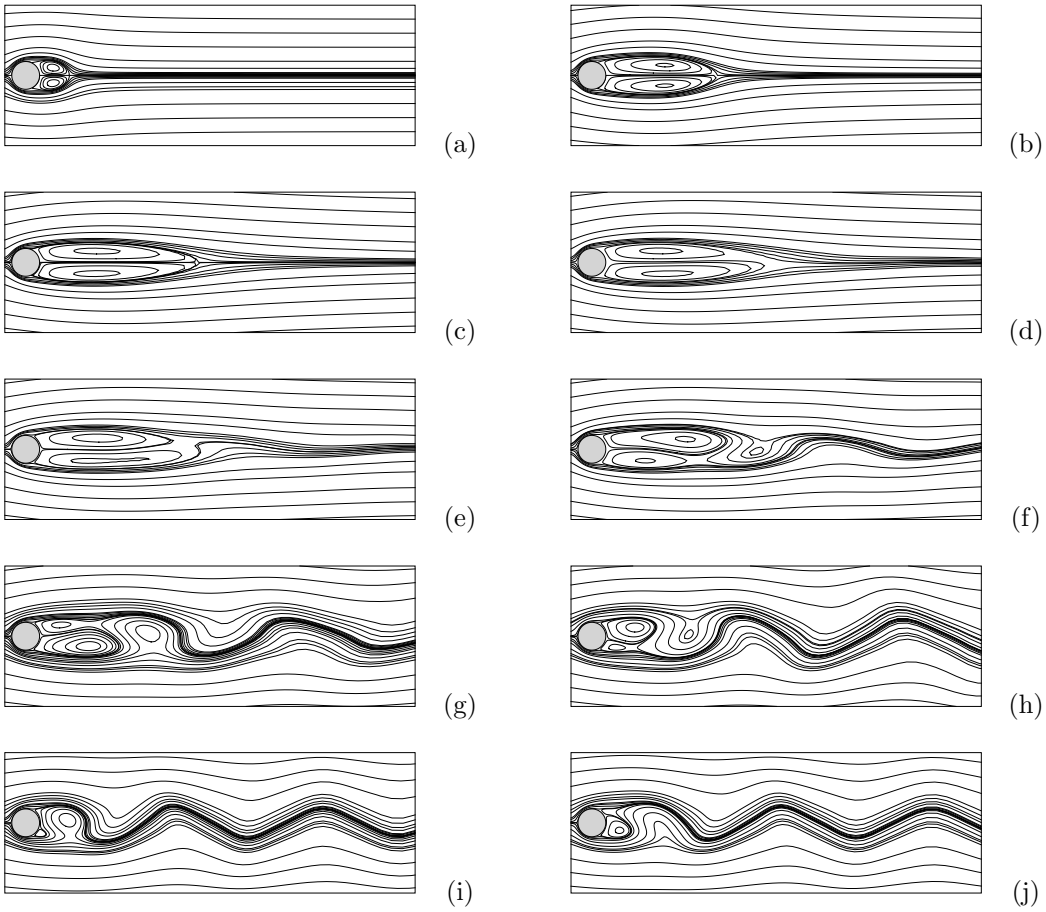

Fig. 5.6: Evolution of steamlines for $Re = 100$ at (a) $t = 2.5$, (b) $t = 15$, (c) $t = 40$, (d) $t = 60$, (e) $t = 70$, (f) $t = 80$, (g) $t = 90$, (h) $t = 100$, (i) $t = 150$ and (j) $t = 200$.

Analyzing the characteristics of the streamlines and sreaklines behind a circular cylinder during vortex shedding is one of the key objectives of this section. For proper insight of the flow field characters it is necessary to visualize both streamlines as well as streaklines. In this regard, we have portrayed the post-processed steady-state contours of streamfunction, vorticity and streaklines for $Re = 100$, 200 and 300 in Fig. 5.9. The steamlines and vorticity contours shown in the figure corresponds to

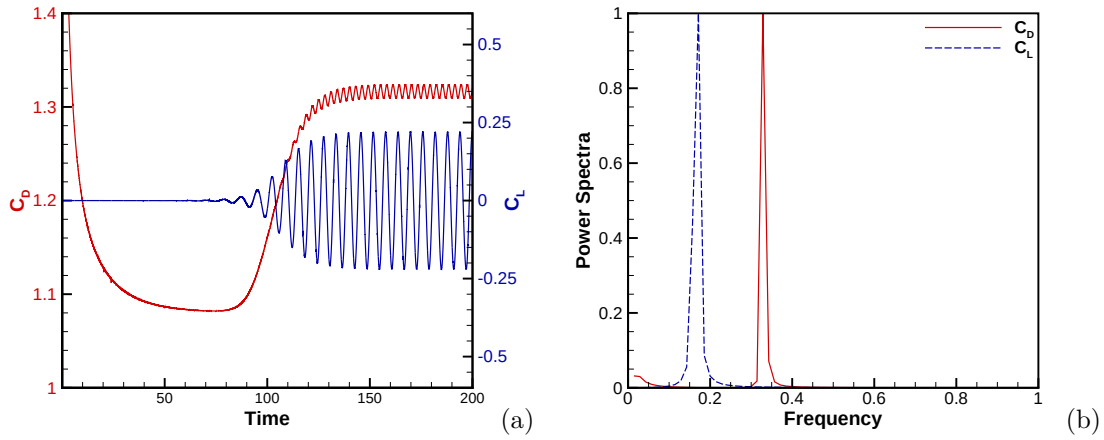

Fig. 5.7: (a) Temporal evolution of C_D and C_L; (b) Power spectrum of C_D and C_L for $Re = 100$.

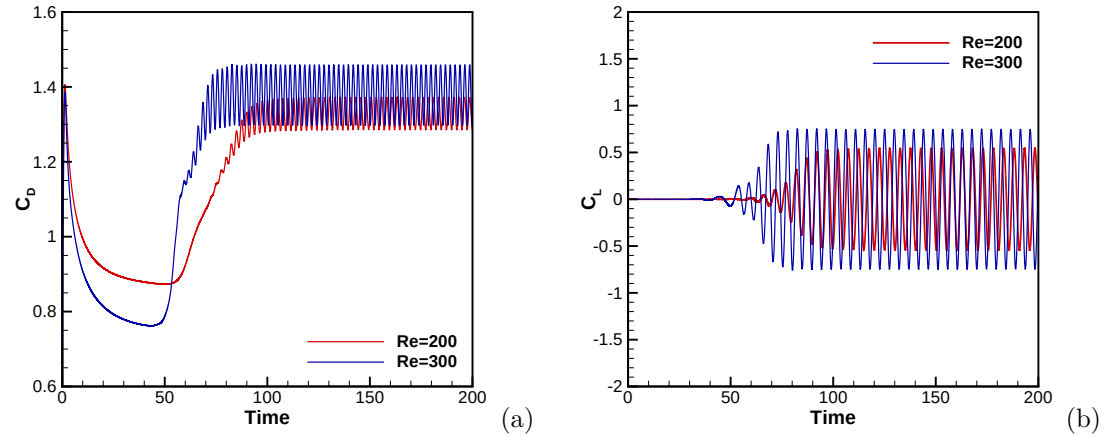

Fig. 5.8: Temporal evolution of (a) C_D and (b) C_L for $Re = 200$ and 300.

a point when C_L attains its peak value for temporally periodic solution. As can be seen in Fig. 5.6a–5.6c, at the beginning of the flow, the wake is in form of a closed loop. However, this closed structures becomes open as vortex shedding starts and fluid flows in from the surrounding. Although the streaklines thin down at this stage, they remain continuous without breakage in Fig. 5.9. In other words, streaklines work as flexible barriers which can never be traversed by the fluid. The surrounding fluid enters the wake from both the sides and moves towards the cylinder surface eventually being driven out of the wake. Once shed, the vortices are carried away by the flowing fluid. The two sets of vortices entwine each other in the downsrtream

region which is accurately portrayed in Fig. 5.9a(ii), 5.9b(ii), and 5.9c(ii). Once vortex shedding starts, the vortices are shed alternatively from the two sides of the cylinder in a periodic manner. This is also evident from the crests and troughs in the streamlines shown in Fig. 5.9a(i), 5.9b(i) and 5.9c(i). These figures also depict the alternative positive and negative values of ω of the eddies present in Fig. 5.9a(ii), 5.9b(ii) and 5.9c(ii) respectively. Moreover, we see that if we increase the Reynolds number the vortex shedding takes place in a more frequent manner. Additionally, in incompressible flows, the vorticity is generated only at the solid boundary, in this case the cylinder surface, and this vorticity remains inside within the fluid. In Fig. 5.9, the streaklines presented also provide a clear view of the spots in the flow field where the vorticity is intrinsic. A qualitative comparison of our numerically computed streakline for $Re = 105$ with the experimental streakline provided by Taneda in [153] is carried out in Fig. 5.10. A close resemblance of essential features in our computed streakline pattern can be seen with the same referred from the literature.

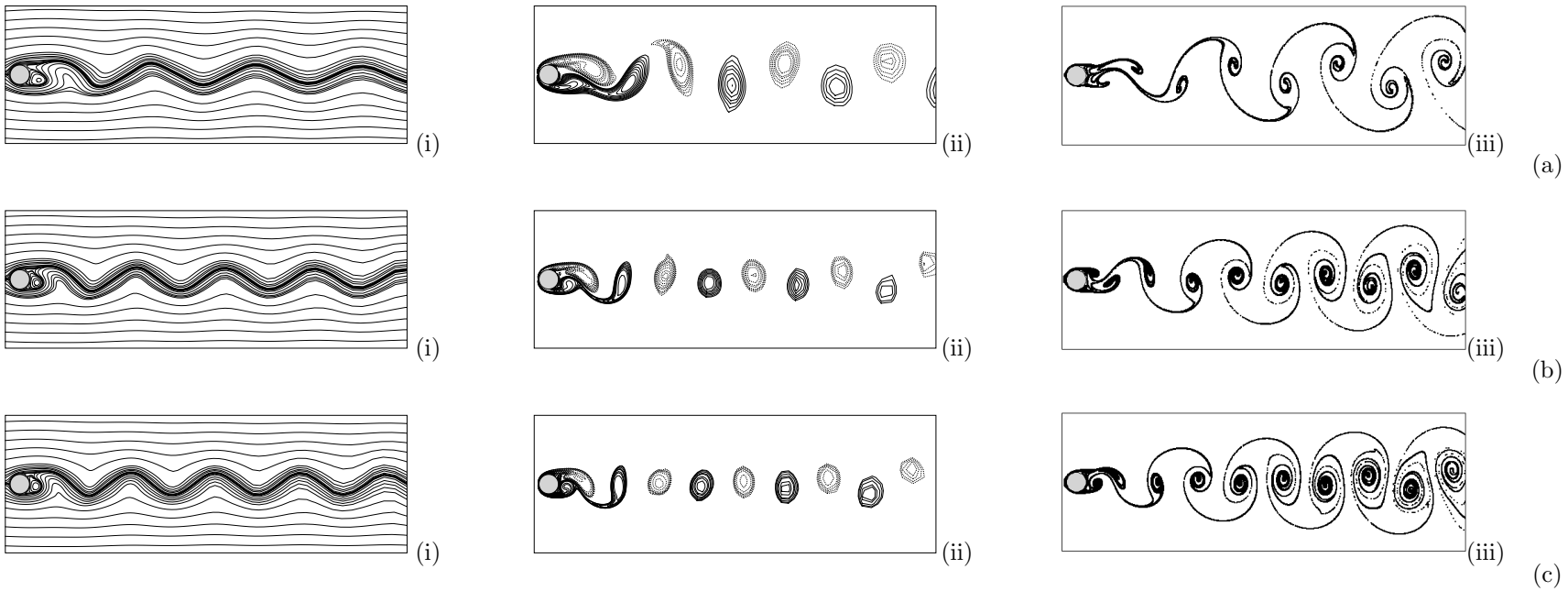

Fig. 5.9: Steady-state streamlines (left), vorticity contours [negative values are represented by dotted lines] (middle) and streaklines (right): (a) $Re = 100$, (b) $Re = 200$, (c) $Re = 300$.

Table 5.4: Comparison of Strouhal number, drag coefficient and lift coefficient of steady periodic flow for $Re = 100$, 200 and 300.

	$Re = 100$			$Re = 200$			$Re = 300$		
	St	C_D	C_L	St	C_D	C_L	St	C_D	C_L
[43]				0.194	1.31	± 0.65	0.205	1.32	± 0.84
[170]	0.163			0.185			0.203		
[144]	0.160	1.39		0.180			0.200	1.27	
[92]	0.160	1.37 ± 0.009	± 0.323	0.187	1.34 ± 0.030	± 0.430	0.200		
[6]	0.169	1.38 ± 0.010	± 0.340	0.200	1.37 ± 0.046	± 0.700			
[167]	0.170	1.379	± 0.357	0.195	1.262	± 0.708	0.206	1.174	
[129]	0.165	1.394 ± 0.007	± 0.191	0.197	1.357 ± 0.038	± 0.453	0.209	1.401 ± 0.068	± 0.607
[87]	0.162	1.325 ± 0.026	± 0.306	0.200	1.333 ± 0.046	± 0.351	0.210	1.410 ± 0.0645	± 0.620
Present	0.171	1.316 ± 0.007	± 0.219	0.200	1.330 ± 0.042	± 0.542	0.210	1.380 ± 0.0782	± 0.745

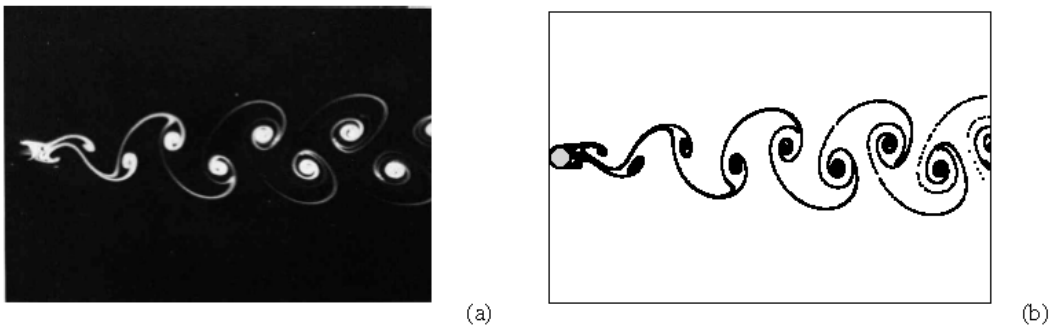

Fig. 5.10: Comparison between the instantaneous streaklines for $Re = 105$ captured in the (a) experimental study of Taneda [153] and (b) present computation.

We further determine the Strouhal number (St) using the formula $St = {}^{fD}/_{U_\infty}$, with f being the dominant frequency of C_L. The dominant frequencies of C_D and C_L are calculated with the help of spectral analysis of temporal evolution of these coefficients. The power spectrums for $Re = 200$ and 300 are shown in Fig. 5.11a. Spectral density analysis clearly establishes that drag coefficient C_D oscillates twice as fast as the lift coefficient C_L. To probe further, we display the phase portrait of C_D and C_L in Fig. 5.11b. Subsequently, we compare our computed values of the parameters St, C_D and C_L with well-established numerical and experimental results for the Re values under consideration. In all the cases we observe very close agreement. The table also indicates that the vortex shedding frequency is directly proportional to Re, which has also been corroborated in Fig. 5.9.

C. Flows for $300 < Re \leq 550$

The numerical simulation of significant features *viz.* (i) the bulge phenomenon and (ii) the secondary eddy phenomenon, is the primary objective of the investigation in this range. These secondary phenomena have been reported in a number of experimental and numerical studies [10, 58, 98, 126].

In the beginning of the flow, distortions in streamlines arise in the regions between vortex separation points and the rear stagnation point. Shortly thereafter, the streamlines near the surface of the cylinder forms a bulge pattern by deviating

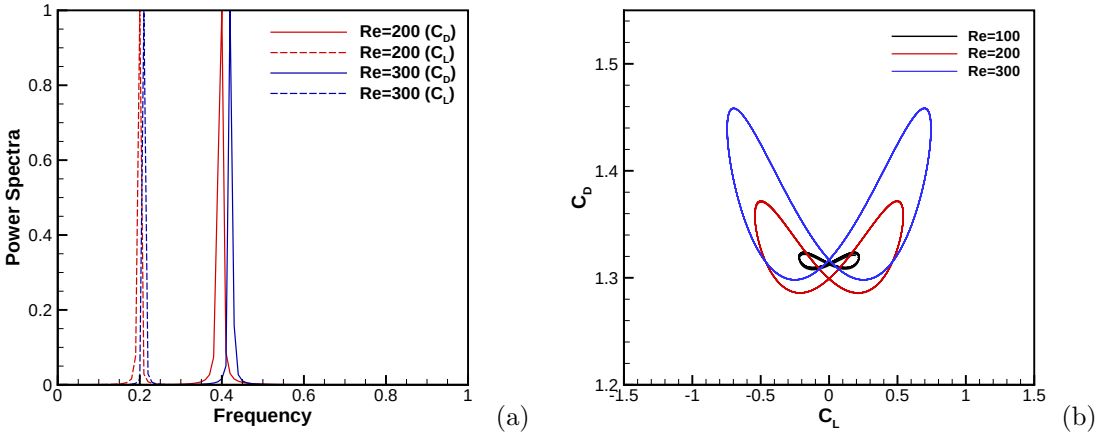

Fig. 5.11: (a) Power spectrum of C_D and C_L for $Re = 200$ and 300; (b) Phase portrait of C_L vs C_D for different Re's.

from the cylinder, commonly referred to as the bulging phenomenon. By accurately computing the instant at which the surface vorticity curve touches the $\omega = 0$ line, the time of occurrence of this secondary phenomena can be determined. Fig. 5.12a and 5.12c reveal that the bulge phenomenon for $Re = 300$ and 550 can be seen approximately at time $t = 2.0$ and $t = 1.3$ respectively (red colored curves). To visualize the phenomenon further, we have presented the streamlines for $Re = 300$ and 550 at their respective times in Fig. 5.12b and 5.12d.

In flows with $Re > 300$, over time, the bulge brings about another flow separation to form a small secondary eddy which rotates opposite to that of the primary vortex. This event is called the secondary eddy phenomenon. We can clearly see the appearance of a pair of secondary vortices for $Re = 550$ at time $t = 1.5$ which is presented in Fig. 5.13a. As can be seen in Fig. 5.13, the secondary vortices gain strength and size as time advances. Moreover, the existence of secondary eddies can be confirmed from the surface distribution of vorticities presented in Fig. 5.12a and 5.12c as well, where two successive changes of sign of a graph implies the existence of a vortex. Fig. 5.12c evidently proves the presence of the secondary vortex phenomena for $Re = 550$ at $t = 1.5$ which sustains for later part of the simulation too as the corresponding graphs traverse $\omega = 0$ line twice (black colored curves). The secondary eddy phenomenon is clearly absent in Fig. 5.12a for $Re = 300$.

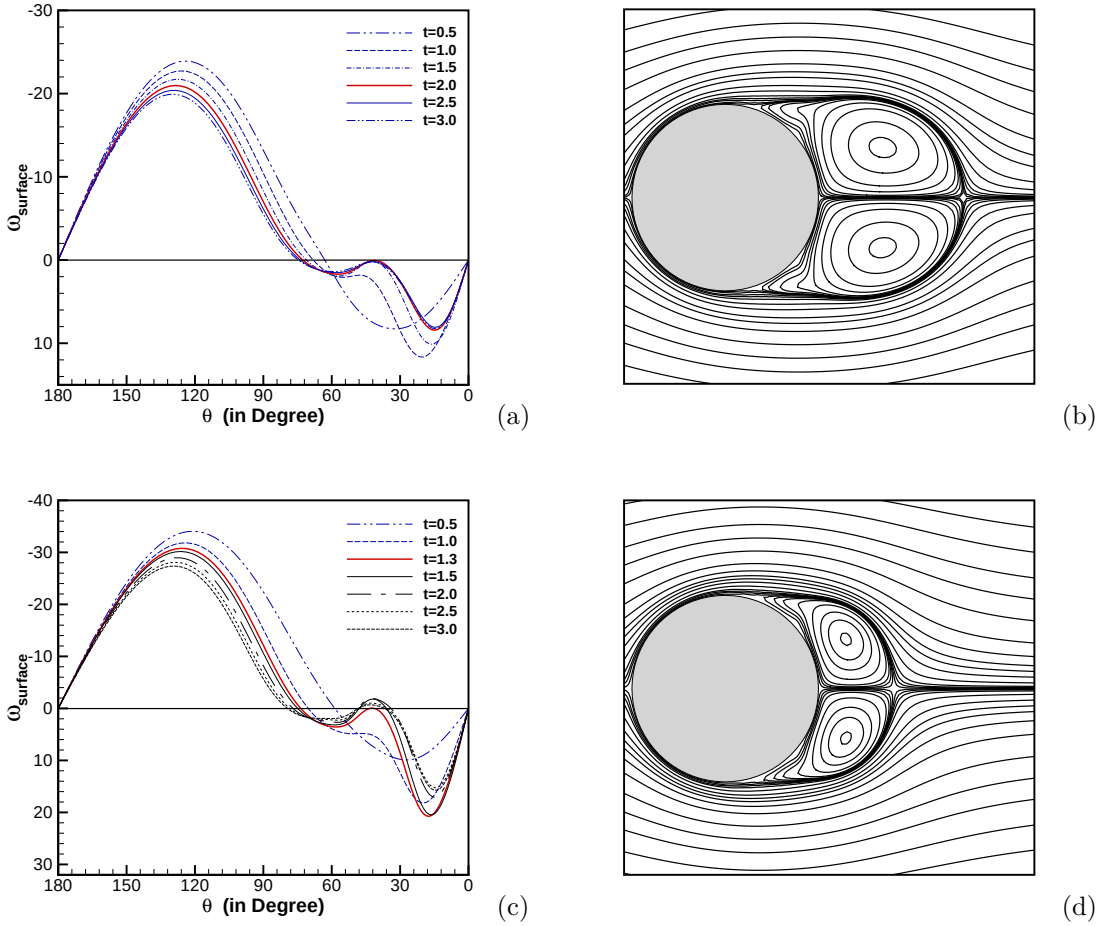

Fig. 5.12: The bulge phenomenon: (a) Time evolution of surface vorticity and (b) streamlines at $t = 2.0$ for $Re = 300$; (c) Time evolution of surface vorticity and (d) streamlines at $t = 1.3$ for $Re = 550$.

A qualitative comparison of our numerically computed streamlines with the experimental results of Bouard and Coutanceau [10] for Re values 300 and 550 at time $t = 2.5$ has been presented in Fig. 5.14. These figures exemplify the extreme closeness between present numerical solutions with the experimental ones, hence validating the adaptability of the present scheme. The parameters l_{max} and $x_{l_{max}}$ at the beginning of the flow for $Re = 550$ along with the experimental results [10] have been compiled in Table 5.3. Further for $Re = 550$, values of the radial velocity u along the line $\theta = 0$ behind the cylinder has been compared with the same reference in Fig. 5.15a. It is heartening to see very close resemblance between the present numerical results and well established experimental results.

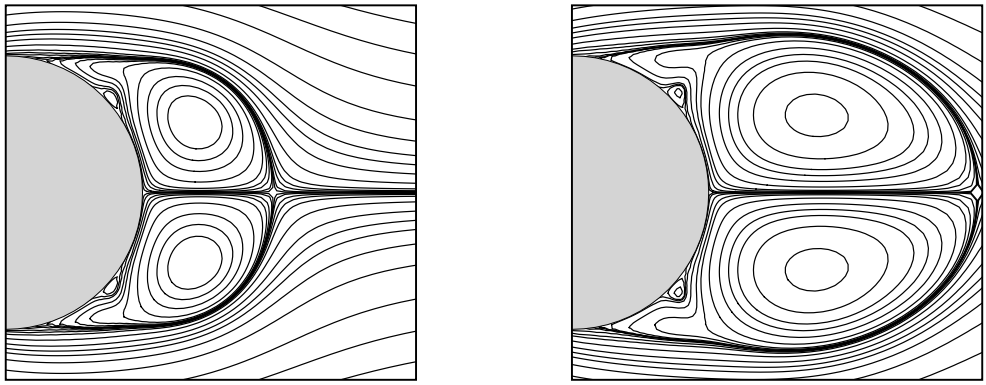

(a) (b)

Fig. 5.13: The secondary eddy phenomenon: Streamlines for $Re = 550$ at (a) $t = 1.5$ and (b) $t = 3.0$.

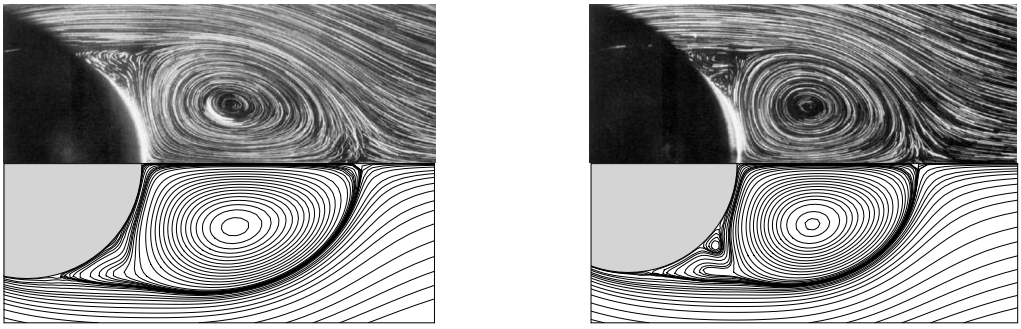

(a) (b)

Fig. 5.14: Experimental streamlines (top half) from [10] and numerically estimated streamlines (bottom half) at nondimensional time $t = 2.5$: (a) $Re = 300$, (b) $Re = 550$.

D. Flows for $1000 \leq Re \leq 9500$

For Re values beyond 550, flow around circular cylinder eventually becomes 3D and turbulent. However, experimental studies show that the flow is still laminar during the early stages of the flow. The primary focus of this range is to simulate the flow near the cylinder wall for an early time span. In this range of Reynolds number, the solution experiences interesting flow phenomena *viz.* α, β, sub-α and sub-β. The α-phenomena, although was first witnessed in the numerical and experimental investigations of Thoman and Szewczyk [155] and Honji and Taneda [62] in 1969,

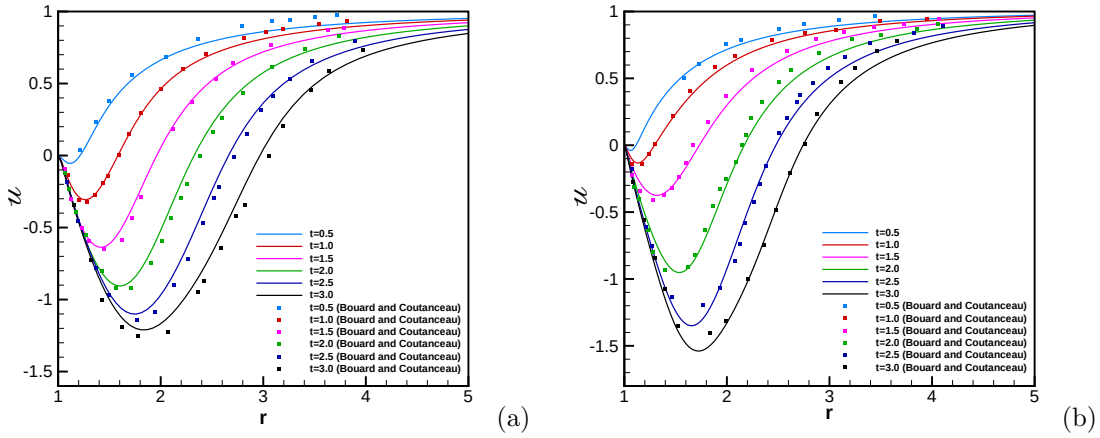

Fig. 5.15: The radial velocity distribution on $\theta = 0$ line behind the cylinder at different instants of the flow and comparison with experimental results from [10]: (a) $Re = 550$, (b) $Re = 3000$.

was coined by Bouard and Coutanceau [10] later in 1980. Over the few years, the presence of α- and β-phenomena in the secondary level was documented in several works [69, 72, 74, 98, 99, 126]. Of late, the existence of α- and β-phenomena at tertiary level has been reported by Kalita and Sen in [73, 74], where they have termed these as sub-α- and sub-β-phenomena. In the present study, we restrict our discussion to secondary α- and β-phenomenon only.

For $Re = 1000$, we have portrayed the evolution of streamlines in Fig. 5.16. The secondary eddy phenomenon for this value of Reynolds number takes place shortly after time $t = 1.0$ and it becomes distinct at $t = 1.25$ in Fig. 5.16c. This secondary eddy gradually gets bigger to an extent for its exterior boundary to touch the boundary of the primary vortex and splits the primary vortex into two parts. We can see the separation of the primary vortex at $t = 1.5$ in Fig. 5.16d. As time progresses, these two secondary vortices become equivalent in strength and size and constitute a pair. This phenomenon is known as the α-phenomenon. Flow for $Re = 1000$ exhibits the α-phenomenon at $t = 2.0$ as can be seen in Fig. 5.16e. These observations are also substantiated by Fig. 5.18a where we have depicted the distribution of surface vorticity at the same time instants as those of the streamlines shown in Fig. 5.16. Fig. 5.18a shows that the curve of surface vorticity changes its

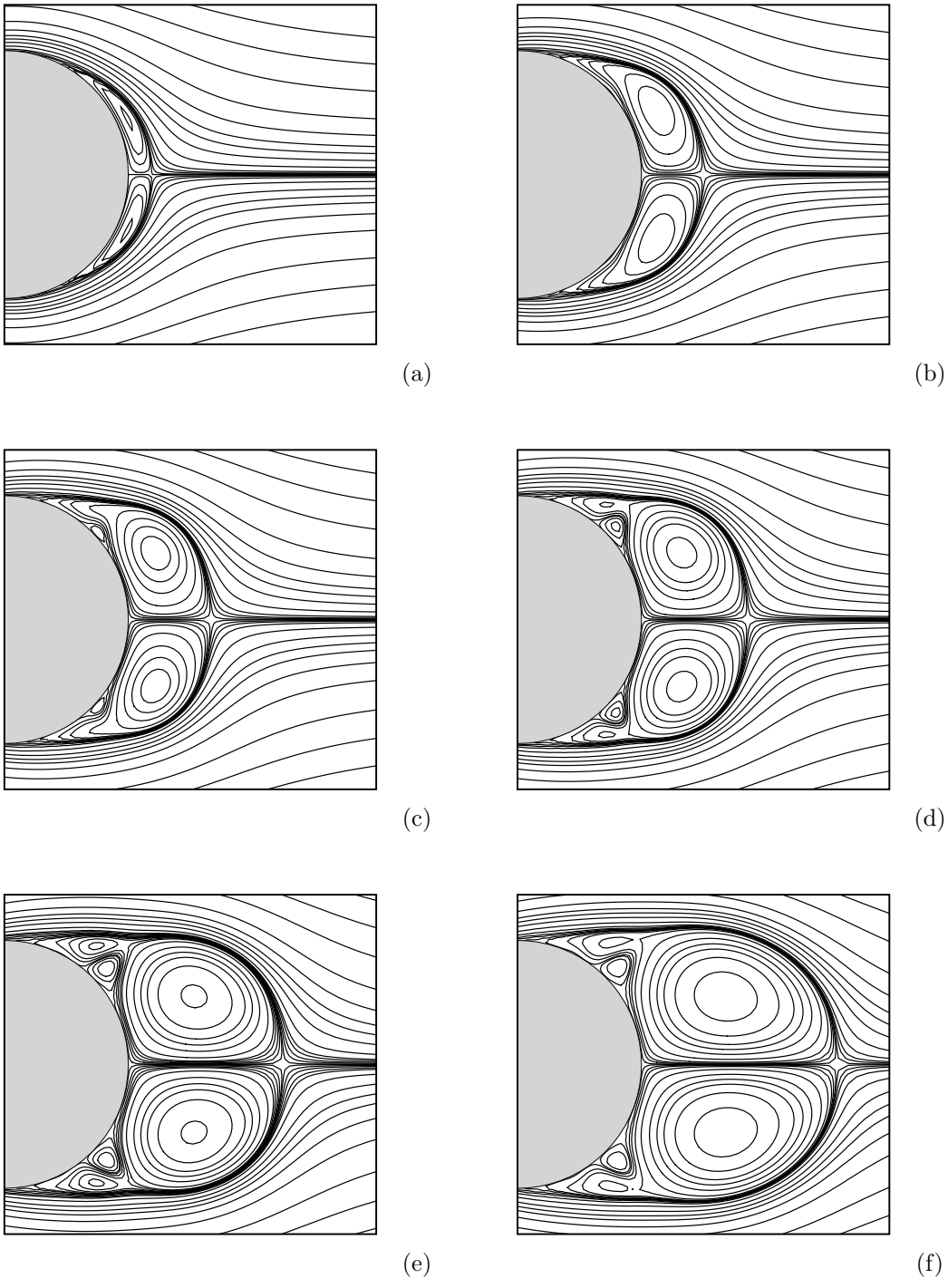

Fig. 5.16: Evolution of steamlines for $Re = 1000$ at (a) $t = 0.5$, (b) $t = 1.0$, (c) $t = 1.25$, (d) $t = 1.5$, (e) $t = 2.0$ and (f) $t = 2.5$.

sign thrice at time $t = 1.25$ indicating formation of two secondary vortices inside the region $\theta \in (36^\circ, 77^\circ)$ (black colored curves). These secondary eddies ultimately become equal in size and strength approximately at $t = 2.0$ (red colored curve).

Flow field for Reynolds number more than 1000 is found to be immensely complex and as such, we concentrate on the flow behaviour near the cylinder's wall only. Here, we fixed the outer boundary at $R_\infty = 8R_0$ and employed a grid of size 193×361 on the computational domain for the simulations of Re = 3000, 5000 and 9500. The effect of this change in far-field boundary on the computed solution is presented in Table 5.5. In the table, we have compiled the value of the parameters L and θ_s at three different times t = 1.0, 1.5 and 2.0 when R_∞ is at $8R_0$ and $45R_0$ for $Re = 5000$. Note that the simulation with $R_\infty = 45R_0$ uses a grid of size 193×321. The table suggests that the effect of grid size and computational domain brings an insignificant variation on the flow structure. The %-difference in both L and θ_s are seen to be much less than 10 as we change R_∞ from $45R_0$ to $8R_0$, which drops even further in the later part of the flow.

Table 5.5: Effect of domain modification on wake length an separation angle at different times for $Re = 5000$.

	$t = 1.0$		$t = 1.5$		$t = 2.0$	
	L	θ_s	L	θ_s	L	θ_s
$R_\infty = 8R_0$	0.229	81.767	0.615	87.330	1.103	88.097
$R_\infty = 45R_0$	0.219	77.563	0.634	84.944	1.107	88.748
%-diff.	4.566	5.420	2.997	2.809	0.361	0.733

Now, we advance our investigation by computing the flow for Re = 3000. The value of flow parameters l_{max} and $x_{l_{max}}$ for Re = 3000 at the early span of the flow are compared with the existing results [10] in Table 5.3. In Fig. 5.15, we have compared the distribution of radial velocity u along $\theta = 0$ line behind the cylinder at different times with those reported in the same experimental study. Similar to the cases for Re = 200 and 550, yet again the numerical solutions appear to be strikingly similar to the experimental ones for Re = 3000. Fig. 5.17 presents the streamlines of the flow at different instants. From the streamlines one can clearly witness the presence of the α-phenomenon for Re = 3000. Fig. 5.17a and 5.17b captures the formation of secondary eddy and the α-phenomenon for $Re = 3000$ at much earlier time than that of $Re = 1000$. This analysis is further supported by the surface vorticity contours portrayed in Fig. 5.18b.

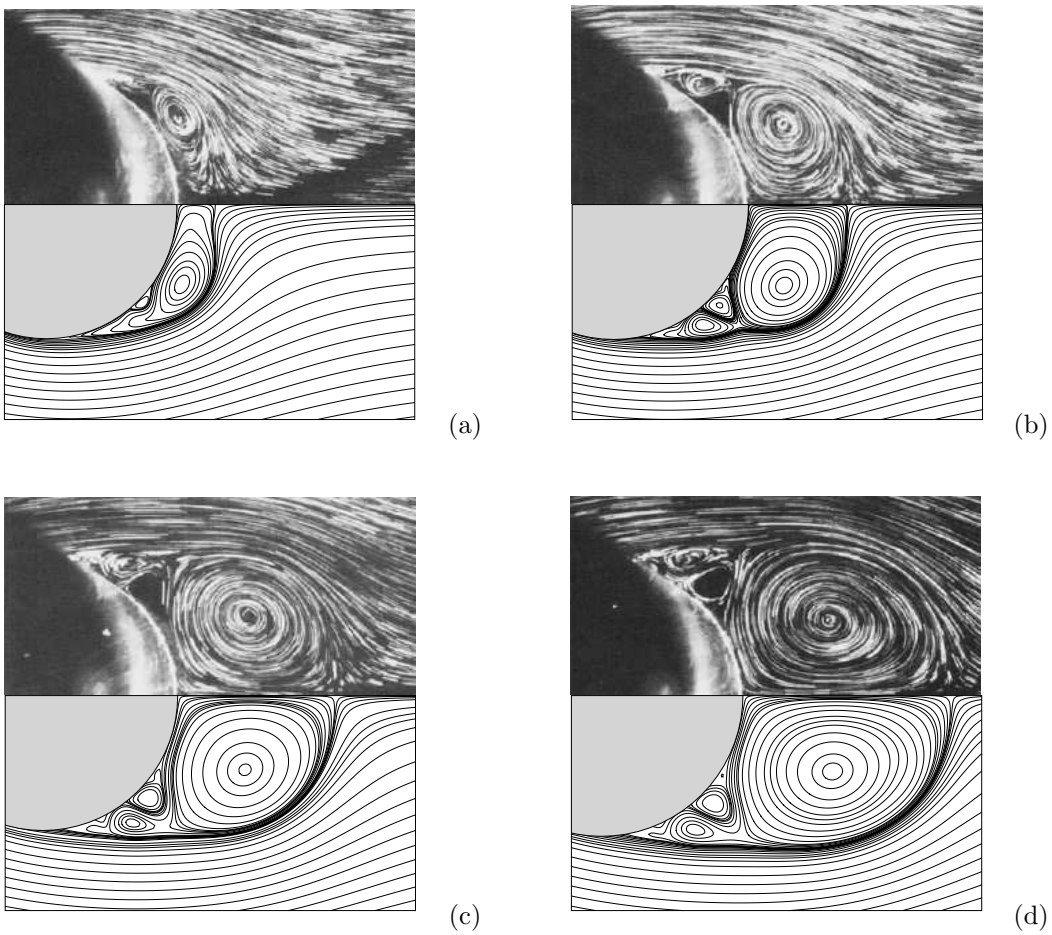

Fig. 5.17: Experimental streamlines (top half) from [99] and numerically estimated streamlines (bottom half) for $Re = 3000$ at (a) $t = 1.0$, (b) $t = 1.5$, (c) $t = 2.0$ and (d) $t = 2.5$.

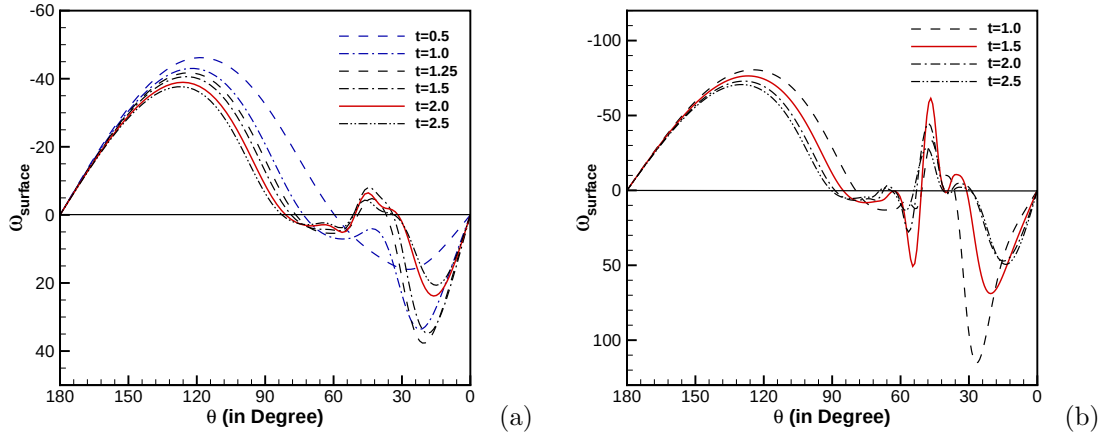

Fig. 5.18: Time history of surface vorticity: (a) $Re = 1000$, (b) $Re = 3000$.

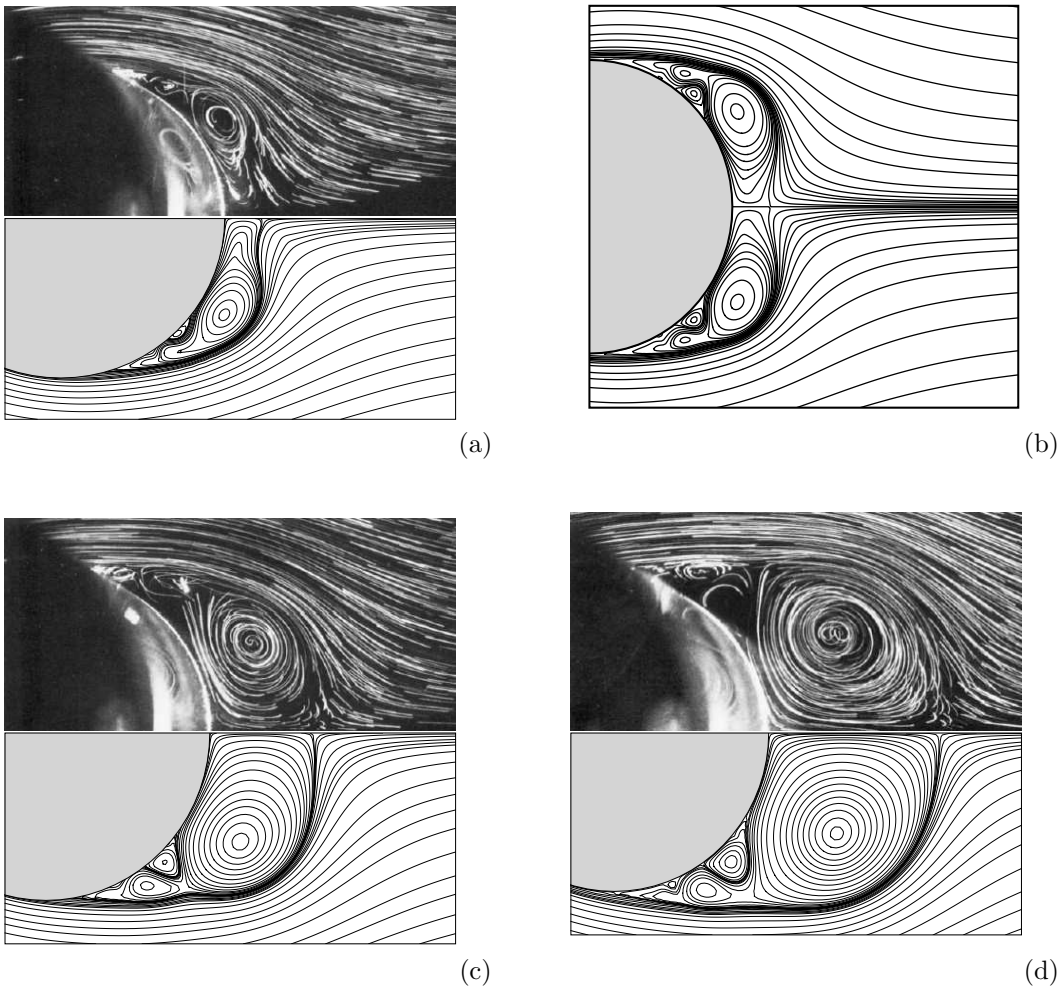

Fig. 5.19: Evolution of streamlines for $Re = 5000$ at (a) $t = 1.0$, (b) $t = 1.15$, (c) $t = 1.5$ and (d) $t = 2.0$ with experimental snapshots from [10] wherever available.

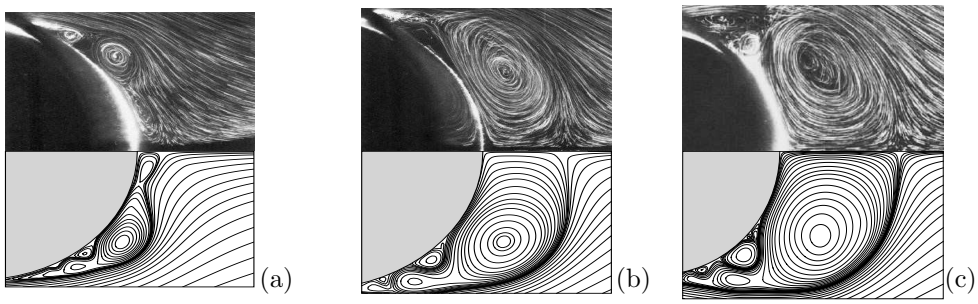

Fig. 5.20: Evolution of streamlines for $Re = 9500$ at (a) $t = 1.0$, (b) $t = 1.5$ and (c) $t = 2.0$ with experimental snapshots from [10].

Next, we extend our numerical scheme to study the flow past a circular cylinder for $Re = 5000$ and 9500. In Fig. 5.19 and 5.20, we have arranged the streamlines

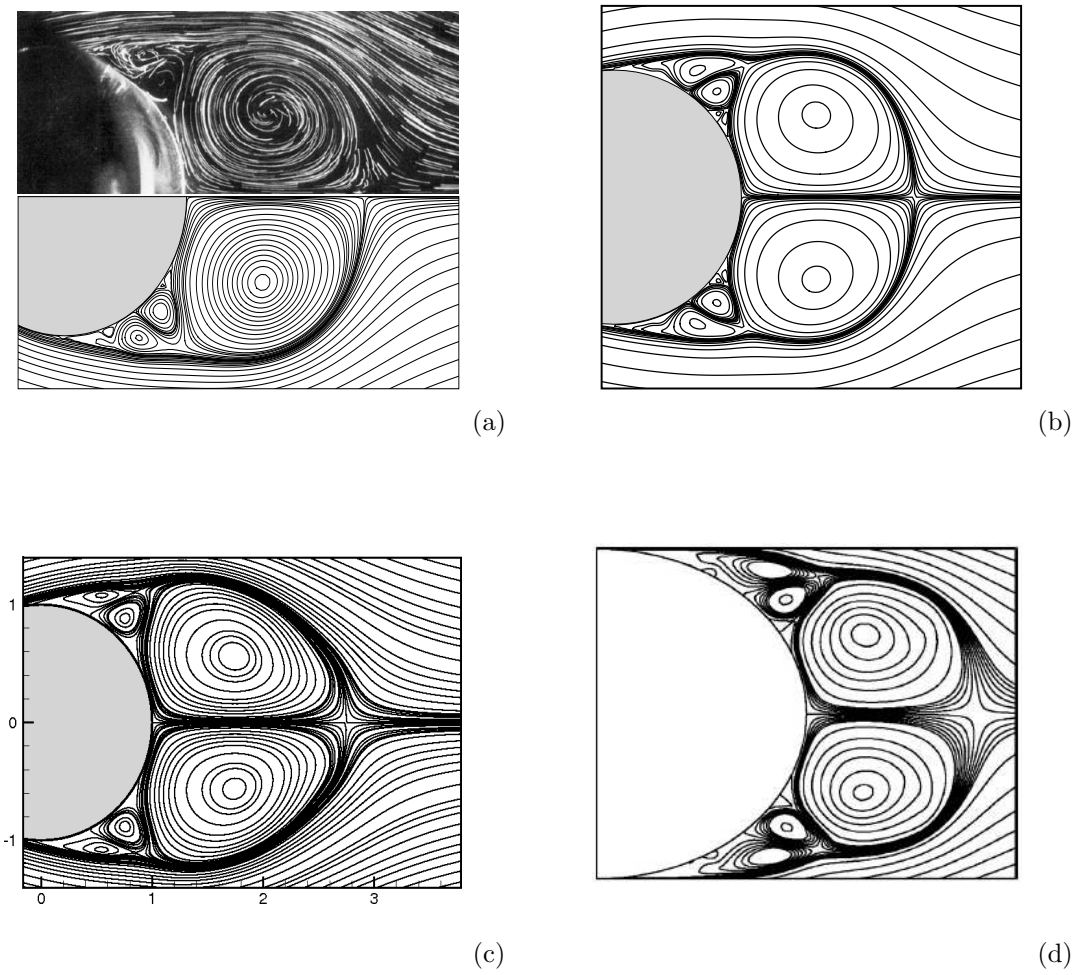

Fig. 5.21: Streamlines for $Re = 5000$ at time $t = 2.5$: comparison with (a) experimental study [10] and numerical studies (b) Kalita and Sen [72], (c) Kalita and ray [69] and (d) Sanyashiraju and Manjula[126].

at different time instants for $Re = 5000$ and 9500 respectively. This flow range is characterised by the important feature known as the β-phenomenon. For these Re values, a very narrow recirculating wake attached to the surface of the cylinder is created at a very early stage due to back flow near the cylinder. As the flow develops further in the downstream region, the core of this recirculating zone rotates at a faster speed than the alternative part of the separated zone, developing a secondary vortex which gains strength and size quickly. Soon afterwards, this secondary vortex separates the primary vortex into two parts, one of which is the core. Although separated, the smaller part maintains a connection with its core. Soon afterwards,

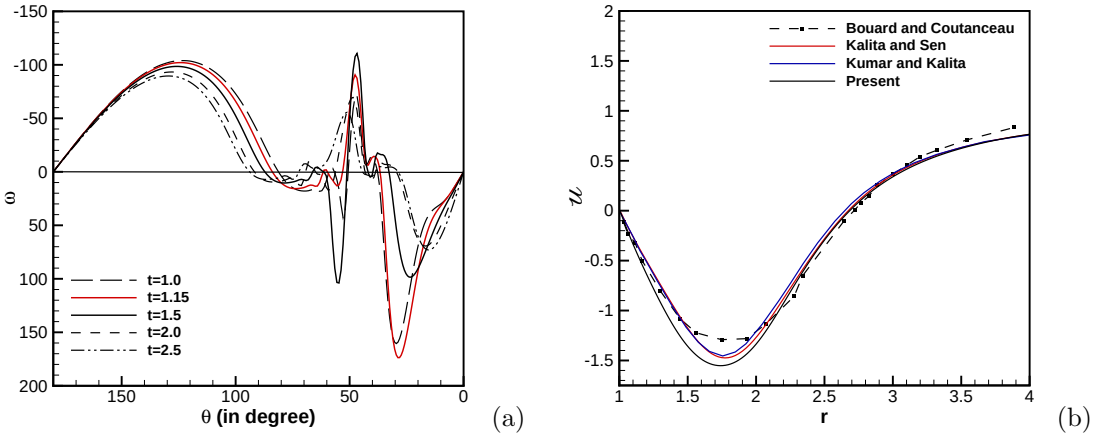

Fig. 5.22: (a) Distribution of surface vorticity for $Re = 5000$ at different instants and (b) the radial velocity distribution on $\theta = 0$ line behind the cylinder and comparison with numerical and experimental results from [10, 73, 87] for $Re = 5000$ at nondimensional time $t = 3.0$.

the channel connecting the two parts of the primary vortex becomes confined due to the strengthening of the secondary vortex. As the flow develops further, the primary vortex gains strength and both of its parts overpower the secondary vortex. This so called β-phenomenon is clearly visible at around time $t = 1.15$ in Fig. 5.19b for $Re = 5000$ and $t = 1.0$ for $Re = 9500$ in Fig. 5.20a. Despite portraying the same visualization in the vicinity of the separation point, the α- and β-phenomena are treated as two distinct features owning to their different fundamentals. For the flow evolution depicted in Fig. 5.19, we can conclude that for $Re = 5000$ the β-phenomenon swiftly transforms to the α-phenomenon detailed earlier in this section, which can be seen in Fig. 5.19b and 5.21a. However, due to the higher instability of the flow, no evidence of the α-phenomenon has been established for $Re = 9500$ (see Fig. 5.20b and 5.20c).

In Fig. 5.19 and 5.20, we have also carried out a qualitative comparison of the present numerical solutions with the experimental results reported in [10], where the upper half of the figure contains the experimental snapshots, and the lower half shows the numerically simulated ones. Yet again, it is heartening to see that our computations could capture the flow as accurately as the experimental study in all the cases. Further, a comparison is carried out between present numerical

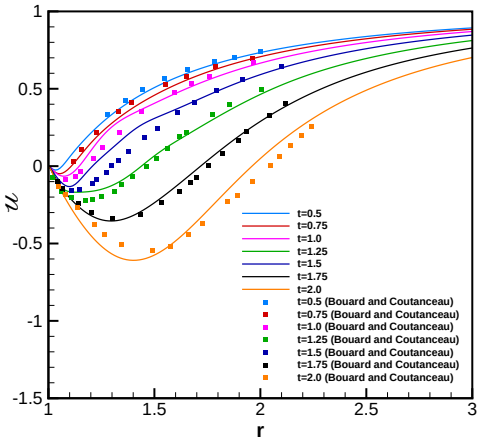

Fig. 5.23: The radial velocity distribution on $\theta = 0$ line behind the cylinder and comparison with experimental results from [10] for $Re = 9500$ at different instants of the flow.

results and numerical results obtained in the works [69, 72, 126] in addition to the experimental results from [10] in Fig. 5.21. Our simulation was able to apprehend the shape and location of the vortices with the highest accuracy even for secondary level. The presence of α- and β-phenomena for $Re = 5000$ becomes evident from the surface distribution of vorticities shown in Fig. 5.22a. Further, we present the velocity distribution for $Re = 5000$ at nondimensional time $t = 0.3$ in Fig. 5.22b. In the figure, we also present a comparison of the present data with the existing results reported in the studies [10, 73, 87]. It's heartening to notice that the accuracy of the present numerical result is comparable of that of the other numerical results taken from [73, 87] in contempt of utilizing a relatively smaller stencil. This attributes to the adaptability of nouniform discretization, which allows the clustering of grids along the line $\theta = 0$. Fig. 5.23 shows excellent proximity between numerical and experimental results for the velocity distribution on $\theta = 0$ behind the cylinder for $Re = 9500$.

5.5 Conclusion

The classical problem of transient viscous incompressible flow past an impulsively started circular cylinder has been studied comprehensively over the years.

The availability of finite difference based HOC schemes to tackle nonrectangular geometries, particularly in polar coordinates, without involving any grid transformation is limited in the literature. In the present study, we perform an extensive investigation of the flow around an impulsively started circular cylinder using a compact scheme which is well capable of handling nonuniform polar grids without any transformation. It is to mention that the scheme is second-order accurate both spatially and temporally. Simulations are carried out for different values of Reynolds numbers ranging from 10 to 9500. This includes simulation until steady state for low Reynolds numbers and simulation during the initial stages in case of moderate and high Reynolds numbers. Detailed discussion is given to the typical flow characteristics for certain subranges of the investigated Re values. The computed results are compared and found to be in excellent agreement with the already established experimental and numerical results. The present investigation not only captured the stable periodic flows for $100 \leq Re \leq 300$, but also the critical secondary events termed as α- and β-phenomena for higher Re's to an satisfactory extent, thereby claiming the robustness of the present scheme.